Assessing Effects of Azimuthally Oriented Roughness on Directional Reflectance of Sand

Greg Badura, Charles M. Bachmann, *Senior Member, IEEE,*

***Abstract*—We measure and compare hyperspectral BRFs of a sand sample of varying roughness levels using the Goniometer of the Rochester Institute of Technology-Two (GRIT-T). We developed a geotechnical routine to generate sand samples of approximately constant density and grain size distribution, but varying roughness levels. In addition, we developed sand samples of two different classes of surface roughness: wave-like and normally-distributed. The samples exhibiting normally distributed roughness met several criterion outlined by Hapke in the roughness correction to his photometric model for a smooth sediment surface. We developed a method to empirically forward model the photometric model for a rough surface using roughness metrics derived from digital elevation models of the surface. Our results from empirically forward modeling the correction factor indicate that Hapke's shadowing function does not adequately describe the effects of macroscopic roughness at a sub-centimeter scale. In addition, we also performed experiments in which we oriented the surface waves of the wave-like roughness profiles in different orientations to the principal plane of illumination. These results indicate that future photometric models of wave-like roughness should include a description of how multiple scattering increases reflectance within cavities, reducing the effects of shadowing within the cavities. Our results also suggest that since Hapke's model correction for macroscopic roughness assumes that the underlying distribution of surface slopes does not depend on azimuth, it can not adequately characterize surface roughness when it is both structured and has a preferred orientation.**

***Index Terms*—hyperspectral, goniometer, radiative transfer, Hapke model, roughness correction, surface roughness, sediment, bi-directional reflectance factor (BRF), bi-conical reflectance factor (BCRF), GRIT-T, digital elevation model (DEM)**

I. Introduction

An important goal in the field of remote sensing is to obtain quantitatively accurate models that relate the scattering of light to physically derived parameters of the surface being imaged. There are many parametric reflectance models that describe the empirically observed interactions of light with particulate media. Certain models account for the macroscopic roughness of the surface through the use of an explicit roughness parameter [1], [2]. Hapke[1] proposed a photometric roughness function that serves as a multiplicative correction factor for the photometric model of a smooth surface. Hapke's model for the photometric reflectance from a rough surface depends not only on incidence, emission, and phase angles, but the effective tilts of surface microfacets [1].

G. Badura is a PhD candidate in Imaging Science at the Rochester Institute of Technology, Rochester, NY, 14623 (e-mail: gpb6751@rit.edu).

C. M. Bachmann is the Frederick and Anna B. Wiedman Chair, Associate Professor, and Graduate Program Coordinator in the Chester F. Carlson Center for Imaging Science at the Rochester Institute of Technology, Rochester, NY, 14623 (e-mail: bachmann@cis.rit.edu).

Manuscript received XXXX,XX, 2018; revised XXXXX,XX, 2018.

There have been many reflectance models created to capture the effect of either periodic or random roughness on the reflectance from a sediment surface. Cierniewski et al proposed models to predict the reflectance from surfaces composed of soil clods using periodic equally sized ellipsoids on a flat horizontal surface [3], [4], [5]. The results of fitting the parameters of this model to experimental field data showed that the model was able to accurately describe the principal plane reflectance of soil surfaces as a function of ellipsoid shape and a soil-clod spacing interval. They found that for high solar zenith angle values, surfaces with greater gaps between spheroids (defined by the authors to be of a lower order of roughness) exhibited lower variance in reflectance along the solar principal plane across different zenith angles [3]. Bechmann developed another model for characterizing the photometric effect of roughness in microwave remote sensing [6]. In this model, the surface of interest is considered to be a stationary process, characterized by a Gaussian height distribution and a surface autocorrelation function. The Hapke photometric model is a physically based model that was developed originally for astronomy applications. Hapke's model derives a roughness correction factor under the assumption that the surface has a random structure with a slope angle distribution that is characterized by Gaussian statistics that are independent of azimuth angle [7]. While the assumed slope angle distribution angle in Hapke's model depends only on zenith angle, the correction factors are implicitly dependent on both zenith and the relative azimuth angle, $\varphi_i - \varphi_e$ between incident light and observation direction through the phase angle g, which is related to direction cosines of the incident and exit zenith angles, μ_i and μ_e and the relative azimuth angle according to: $g = cos^{-1}(\mu_i\mu_e + \sqrt{1-\mu_i^2}\sqrt{1-\mu_e^2}cos(\varphi_i - \varphi_e))$.

All of the above models operate under the assumption that the orientations of the rough surface microfacets are randomly distributed in azimuth orientation. While sediment surfaces such as fallow agricultural fields or volcanic surfaces exhibit randomly distributed roughness, certain surfaces such as sand dunes or coastal beaches are known to exhibit azimuthally dependent roughness in the form of wavelike ripples [8]. These sites are frequently the focus of remote sensing studies for calibration and validation purposes. For example, [9] developed a simulation environment to model the interaction of light in the Algodones Dunes desert as an intercalibration site for spaceborne instruments. In another study, [10] analyzed the effects of sand dune spatial organization in the Libya-4 desert site on the surface bidirectional reflectance factor using a 3D radiative transfer model, with the surface characterized by azimuthally oriented sand dunes created by the dominant

wind direction. While these studies focus on regions with statistically correlated surface roughness on the order of tens to hundreds of meters, little attention has been paid to the photometric effect of azimuthally-independent roughness on the order of millimeters to centimeters. In this work, we describe laboratory experiments with roughness characterized by centimeter-scale surface distortions within a field of view that is of comparable scale. In recent field studies, this is the same spatial resolution of hyperspectral imagery that we have obtained using a mast-mounted hyperspectral imaging system [11],which can be used in future studies to test our results in the field. While our present study considers an experimental paradigm in which the surface distortion represents a significant fraction of the pixel field of view, we do not address the case of a pixel size significantly larger than the size of the surface distortion, i.e. the effect of averaging over scales much larger than the surface distortion. This will be considered in future work.

In this study, we analyze effects of azimuthally oriented roughness using directional reflectance measurements obtained under illumination conditions from both oblique angles as well as angles close to nadir in a controlled laboratory setting. We outline a geotechnical technique for manipulating the roughness of a sand surface while holding the sediment density and grain size distribution constant. We compare two distinctly different surface roughness characterizations: a surface with periodic mounds, and a surface with directionally oriented surface waves. The surfaces with periodic mounds have no azimuthal preference and therefore satisfy the criterion used by Hapke in his derived correction factor for surface roughness [1].

There have been many radiative transfer inversion studies that attempt to retrieve geophysical parameters from the photometric model for a rough surface [12], [13], [14]. These studies have assumed that the correction factor derived by Hapke is valid for surfaces which are isotropic in facet azimuth distribution. However, there have been few studies that attempt to determine if Hapke's correction factor is valid for macroscopically rough sand surfaces using goniometer measurements. For this reason, we also outline a test to examine how well the correction factor can account for centimeter-scale roughness. While all scales of roughness ultimately play a role in directional reflectance of a surface, several studies have shown that macroscopic surface roughness on the scale of a single particle to the scale of a centimeter is considered sufficient to explain photometric roughness [15], [14].

Using the outlined experimental methodology, this study had three major goals: (1) to assess differences in measured directional reflectance between a sand surface with slopes that are normally distributed and a sand surface with oriented surface waves, (2) to empirically assess the photometric effect of sand surface wave orientation relative to the direction of incident light, and (3) to experimentally assess the ability of the Hapke [1] surface roughness correction factor to account for centimeter-scale surface roughness.

II. Theory

A. Hapke Photometric Model for a Smooth Surface

The Hapke photometric model is an approximate analytical description of the bidirectional reflectance distribution function (BRDF) of a smooth medium composed of particles [7]. It was originally derived to model the reflectance of lunar surfaces, but was extended to retrieve material properties from sediment surfaces through model inversion [14]. Hapke formulated a radiative transfer model that incorporates five orders of scattering [7]. The derived model includes terms for single and multiple scattering as well as the opposition effect (the increased brightness observed at orientations close to the illumination direction) [7]:

$$r(i,e,g) = K\frac{w(\lambda)}{4}\frac{1}{\mu_i+\mu_e} \times \left(p(g)[1+B_{s0}B_s(g,K,\lambda)] + \left[H\left(\frac{\mu_i}{K}\right)H\left(\frac{\mu_e}{K}\right)-1\right]\right) \times [1+B_{c0}B_c(g,K,\lambda)] \quad (1)$$

where $w(\lambda)$ is the single wavelength scattering albedo, $p(g,\lambda)$ is the single scattering phase function at phase angle g, μ_i = $cos(i)$ and μ_e = $cos(e)$ are the direction cosines of the incident and observation zenith angles. The parameter K is the "porosity function," which depends nonlinearly on the sediment fill factor ϕ according to:

$$K \approx -\frac{ln(1-1.209^{2/3})}{1.209^{2/3}} \quad (2)$$

The functions $H(\mu_i/K)$ and $H(\mu_e/K)$ determine the contribution due to multiple scattering in the Isotropic Multiple Scattering Approximation (IMSA) model. The factors $B_{S0}B_S$ $(g,K,)$ and $B_{C0}B_C(g,K,)$ represent corrections for the shadow hiding opposition effect (SHOE), [7], [1] and the coherent backscatter opposition effect (CBOE), $B_{C0}B_C(g,K,)$, [7] respectively.

Hapke extended the photometric model for a smooth surface to include corrections for macroscopic roughness that appear as an overall multiplicative factor $S(i,e,\psi,\bar{\theta})$, where ψ is the relative azimuth angle between solar and observation directions [1], [7].

B. Hapke Roughness Correction for the Smooth Photometric Model

Hapke developed a correction to a photometric function for BRDF of a smooth particulate medium that accounts for effects of macroscopic surface roughness. This macroscopic roughness correction is a function of a single parameter: the mean slope angle $\bar{\theta}$. The mean slope angle parameter is defined by Hapke in (3):

$$\bar{\theta} = tan^{-1}\left(\int_0^{\pi/2} a(\theta)tan(\theta)d\theta\right) \quad (3)$$

where θ is the slope angle of the surface normal of a given surface facet, and $a(\theta)$ is a one-dimensional function describing the distribution of facet slopes in any vertical cut through the

surface at an arbitrary azimuth angle. The slope distribution, $a(\theta)$, can be characterized by the following equations:

$$a(\theta) = \frac{2}{\pi tan^2\bar{\theta}} sec^2\theta sin\theta \exp^{-\frac{tan^2\theta}{\pi tan^2\bar{\theta}}} \tag{4}$$

$$\int_0^{\pi/2} a(\theta)d\theta = 1 \tag{5}$$

where (5) states that the slope distribution function $a(\theta)$ must be normalized over the range of all possible slope angles. It is evident from this equation that the slope distribution function takes on the same form as a probability distribution function of the slope angles of the micro-facets of the surface, a fact that we used to derive the $\bar{\theta}$ factor empirically in Section III-F.

Hapke made several assumptions in deriving a roughness correction for the smooth photometric model [7]:

1) The surface is composed of small, smoothly changing facets that are large relative to the mean sediment grain size.
2) The distribution of facet normal orientations is independent of azimuth angle, so that the slope distribution function $a(\theta, \psi)$ can be written simply as $a(\theta)$, where θ is the zenith angle of the slope normal and ψ is the azimuth angle of the slope normal.
3) Large slope angles due to overhangs and cliffs are absent from the surface.
4) Light multiply scattered from one surface facet to another surface facet is ignored, and only single scattered light is considered in the derivations.

Under these assumptions, Hapke argued that the effects of macroscopic surface roughness on bidirectional reflectance are greatly simplified [7]. In particular, unresolved shadows cast onto surface facets by illuminated surface facets decrease the overall reflectance of the medium. In addition, when the surface is viewed or illuminated at extreme zenith angles, surface facets that are titled away from the observer will be hidden or in shadow. This means that the only surface facets visible to the observer at extreme sensor viewing geometries are those that are tilted preferentially toward the detector while simultaneously being illuminated by the light source [1].

Hapke derived the rough surface bidirectional reflectance, $r_R(i, e, g, \bar{\theta})$, as the product of a shadowing function, $S(i, e, g, \bar{\theta})$, and the bidirectional reflectance of a smooth surface, $r(i_e, e_e, g)$, with effective area A_e [1]. In his model, the bidirectional reflectance of a rough surface can be written as:

$$r_R(i, e, g, \bar{\theta}) = r(i_e, e_e, g)S(i, e, g, \bar{\theta}) \tag{6}$$

The values of effective incident zenith angle, i_e, effective viewing zenith angle, e_e, and the shadowing function, $S(i, e, g)$, are dependent on the relative magnitudes of the incident illumination zenith angle, i, and the sensor zenith angle, e. While the smooth-surface BRDF model in Equation (1) was derived from first principles, Hapke did not derive $S(i, e, g, \bar{\theta})$ from first principles but rather as a multiplicative correction for surface roughness [1].

Hapke [1], [7] derived two different solutions that are dependent on whether i is larger or smaller than e due to shadows being hidden at certain viewing orientations. For example, if the viewer were oriented in the backscatter direction (ψ = 0) with $i \leq e$, then no shadows would be visible and the viewer would only see illuminated facets [1].

When $i \leq e$, the system of equations for calculating the roughness correction factor take on the following forms:

$$\cos(i_e(i, e, \psi)) = \chi(\bar{\theta}))\left(\cos i + \sin i \tan\bar{\theta}\frac{\cos\psi E_2(e) + \sin^2(\psi/2)E_2(i)}{2 - E_1(e) - (\psi/\pi)E_1(i)}\right) \tag{7}$$

$$\cos(e_e(i, e, \psi)) = \chi(\bar{\theta})\left(\cos e + \sin e \tan\bar{\theta}\frac{E_2(e) - \sin^2(\psi/2)E_2(i)}{2 - E_1(e) - (\psi/\pi)E_1(i)}\right) \tag{8}$$

$$S(i, e, g) = \frac{\cos e_e}{\eta(e)}\frac{\cos i}{\eta(i)}\frac{\chi(\bar{\theta})}{1 - f(\psi) + f(\psi)\chi(\bar{\theta})[\cos i/\eta(i)]} \tag{9}$$

When $e \leq i$, the equations take on slightly modified forms:

$$\cos(i_e(i, e, \psi)) = \chi(\tan\bar{\theta}))\left(\cos i + \sin i \tan\bar{\theta}\frac{E_2(i) - \sin^2(\psi/2)E_2(e)}{2 - E_1(i) - (\psi/\pi)E_1(e)}\right) \tag{10}$$

$$\cos(e_e(i, e, \psi)) = \chi(\tan\bar{\theta})\left(\cos e + \sin e \tan\bar{\theta}\frac{\cos\psi E_2(i) - \sin^2(\psi/2)E_2(e)}{2 - E_1(i) - (\psi/\pi)E_1(e)}\right) \tag{11}$$

$$S(i, e, g) = \frac{\cos e_e}{\eta(e)}\frac{\cos i}{\eta(i)}\frac{\chi(\bar{\theta})}{1 - f(\psi) + f(\psi)\chi(\bar{\theta})[\cos e/\eta(e)]} \tag{12}$$

We define the ancillary functions E_2, E_1, χ, η, and f for the above equations in Appendix Section A in (17) through (21). The equations for the roughness correction factor take on complicated forms that are explicitly dependent on both the zenith angle of incident light and the sensor viewing geometry. This means that the correction factors in (7) through (12) must be calculated for every sensor orientation along the hemisphere of the BRDF measurement pattern. In this study, we develop methods to use the empirically measured $\bar{\theta}$ metric of a surface to experimentally forward model (6) for samples that are assumed to have constant sample density but varying levels of macroscopic surface roughness.

III. Methods

A. Goniometer of the Rochester Institute of Technology - Two

The Goniometer of the Rochester Institute of Technology-Two (GRIT-T) uses a dual-view measurement design using two Analytical Spectral Devices (ASD) FR4 spectro-radiometers to simultaneously measure radiance reflected from a target on the ground and downwelled radiance from the sky. The

spectrometers record spectral directional radiance measurements over a range of 350-2500 nm at a spectral bandwidth ranging from 1-3 nm [16]. GRIT-T is designed to be used in both field and laboratory settings. GRIT-T has a rotating sensor-head that accurately tracks its measurement spot in the target plane and mitigates parallax errors [17]. The goniometer also has a slim profile along the sensor head and associated rotation arm that minimizes shadowing onto the measurement spot when the sensor is oriented at or near the opposition direction. By minimizing self-shadowing near the opposition direction, GRIT-T can characterize the theoretical reflectance "hot-spot" [18] more accurately. GRIT-T also incorporates an open ring design to further reduce self-shadowing.

We use the term bidirectional reflectance factor (BRF) to denote that the resulting spectra are the ratio of the reflected radiance from a uniform surface area to the reflected radiance from an ideally diffuse surface of the same area, [19] where the ideal surface was a Spectralon calibration panel. In field settings, the term hemispherical-conical reflectance factor (HCRF) can also be used in this context to denote the fact that the sensor field of view has a finite angular extent and the sources of illumination are both direct and diffuse [19]. In a laboratory setting, the term bi-conical reflectance factor (BCRF) is often used in place of BRF to emphasize the finite extent of both light source and measurement instrumentation.

GRIT-T is equipped with a digital camera system adjacent to the spectrometer fore-optic. GRIT-T obtains a camera image of the target prior to recording each directional radiometric measurement. The camera system is an iDS uEye XS camera with a 5 megapixel CMOS sensor arrangement, and a 60° field-of-view. This camera's pointing axis is parallel to the optical axis of the downward-looking ASD fore-optic. Due to the hemispherical scan pattern of GRIT-T's BCRF measurements, the camera orientations have highly convergent geometries that result in large swaths of feature overlap across output images. We use these resultant images of sediment surfaces as input to structure from motion algorithms [20] [21] [22] [23] in order to obtain a high-resolution digital elevation model (DEM) of the surface.

B. Structure From Motion Photogrammetry

Structure from Motion (SfM) is a method that achieves unsupervised point cloud reconstruction using images of a scene obtained at a variety of geometries. Previous studies have shown that structure from motion tools can be useful for characterizing the roughness of sediment surfaces such as agricultural soils [21]. The basic operating chain of SfM algorithms consists of four major steps: distortion removal from input images using measured camera intrinsics, image feature assignment, feature matching across images, and 3-dimensional reconstruction [23]. A known limitation of SfM point clouds is that they are derived with arbitrary scale and orientation [20]. In order to compensate for this limitation, we insert a reference frame with 4 ground control points to achieve a consistent scaling of the retrieved SfM point clouds.

We use the images of the sediment surface obtained by GRIT-T's camera as input to the open-source SfM program $VisualSFM$, developed by Wu [23] [22]. $VisualSFM$ generates a densely populated point cloud reconstruction using the clustering views for multi-view stereo (CMVS) algorithm. CMVS relies on a graph-cut algorithm which follows a region-growing step which creates a sparse point cloud using only camera poses that observe the same portion of the scene [24]. The $VisualSFM$ program also has a user interface for entering coordinates of ground control points within the scene for point cloud scaling. The program provides error metrics in the form of root mean squared errors (RMSE) between triangulated coordinates and empirically measured coordinates of the ground control points. We compared the RMSE values obtained for 8 different SFM point clouds of sediment samples and found that the triangulation of the $x-$ and $y-$ coordinates was accurate to within 0.10 cm.

C. Sand Sample Preparation and Analysis

We acquired 36 BRF measurements series of a sand sample that was collected during a summer 2017 field campaign. The sample was collected at a beach on the eastern shore of Hog Island, Virgina (37° 24' 58" N, 75° 41' 28" W). BRF measurements were performed in laboratory conditions, which have been shown to be effective in evaluating the directional reflectance properties of rough sediment surfaces at a broad range of illumination conditions [25] [26].

We performed a sieve-shaking analysis of the sample using Humboldt meshes ranging from 25 μm to 4700 μm. We found that the sample was $\sim 90\%$ composed of sand particles in the range of 180 μm to 300 μm, and that the smallest particles in the sediment sample were 75 μm. In addition, we compared these results to sieve shaking analyses of 5 different samples obtained within a radius of $\sim$ 20 meters and found that the samples had similar grain size distributions.

Prior to performing radiometric measurements, we dried the sample for 24 hours at $110° C$ in order to remove excess moisture from the sample. Our goal in this study was to prepare samples that had varying surface roughness but constant sample density. In order to achieve this goal, we developed an approach that relied on using an ASTM standard for pluviation to create constant sample density, [27] and then we created surface roughness using custom-designed grid meshes .

1) Sample Pluviation: Several methods are available for manipulating the density of sediments including tamping, vibration and pluviation. We manipulate sample density using the method of pluviation, defined by the ASTM method $D4253-83$. Pluviation, by definition, is a process consisting of raining cohesionless soil particles onto a sample holder, by using only the force of gravity and using appropriate sieve meshes to act as diffusers [27]. This method consists of allowing sediment particles to freely fall until encountering six sieve meshes acting as diffusers, which are rotated 45° horizontally with respect to each other. The sediment particles then exit the bottom-most sieve mesh and continue to fall until reaching the sample holder. This distance between the bottom-most sieve and the top of the sample holder is denoted as the *Height of Drop* (H_D). The particles are allowed to settle and the surface is finally leveled off to create a perfectly

flat surface. The resultant density of the sediment sample is directly related to H_D due to the imparted kinetic energy of the falling particles. The pluviation method is preferred by the geotechnical community for creating varying densities of sand samples for several reasons, including: uniform spreading of particles throughout the sample holder, accurate creation of densities, and repeatability of density profiles by using the same value of H_D across runs [27].

We developed a custom pluviation device for the purpose of manipulating sediment sample densities. In the first stage of roughness preparation, we pluviated all of the sand samples using a constant H_D = 50 cm. In this manner, all samples had approximately the same density prior to generating roughness patterns, mitigating the potential for varying sample porosity to affect retrieved BCRF measurements. We tested this method by preparing the sand sample via pluviations 15 times from H_D = 50 cm, and found that the resultant densities were constant to within $\sim 1.5\%$.

2) Sand Sample Roughness Preparation: One of our goals for this study was to assess the differences in directional reflectance properties of two different surface roughness profiles: wave-like roughness and normally distributed roughness. We designed custom meshes to create these roughness classes in a repeatable manner. One mesh type had horizontally and vertically oriented bars. This mesh creates a roughness pattern with slopes that do not exhibit azimuthal preference. The other mesh type had only vertically oriented bars that was used to create a wave-like surface roughness profile.

We used meshes with different grating spacings to compare directional scattering effects for sand samples with varying spatial frequencies. In order to examine the role of roughness in the BRF of sediments, we created three different roughness patterns of varying spatial frequencies for both the wavelike roughness mesh and the grid-like roughness mesh. The grating spacing was 25 mm for the coarsest grid, and 10 mm for the least coarse grid. We also used a perfectly smooth sample resulting from the pluviation procedure as a control to isolate the effects of macroscopic surface roughness. The grids used were approximately 20 cm in diameter. For the typical GRIT-T measurement geometry, this diameter ensured that only the roughness pattern would be within the field-of-view of a 5 degree fore-optic at an extreme sensor view zenith angle of 65 degrees.

After performing pluviation, the cone of sand on top of the sample holder was leveled off to create a uniformly smooth surface. In order to create each roughness profile, we pressed a sieve mesh into the sample to a depth of approximately 15 mm and then removed the mesh in a vertical direction from the sample. We made the assumption that this approach creates a sample that is approximately constant in density between runs, so that macroscopic surface roughness was the only variable changed. The resulting images of the roughness profiles are shown in Fig. 1. We denote the samples resulting from using grid-like meshes with grating spacings of 10 mm and 25 mm as *S-Grid10* and *S-Grid25*, respectively. Similarly, we label the samples resulting from using wave-like meshes with grating spacings of 10 mm and 25 mm as *S-Wave10* and *S-Wave25*, respectively. We also label the smooth sand sample as *S-Smooth*.

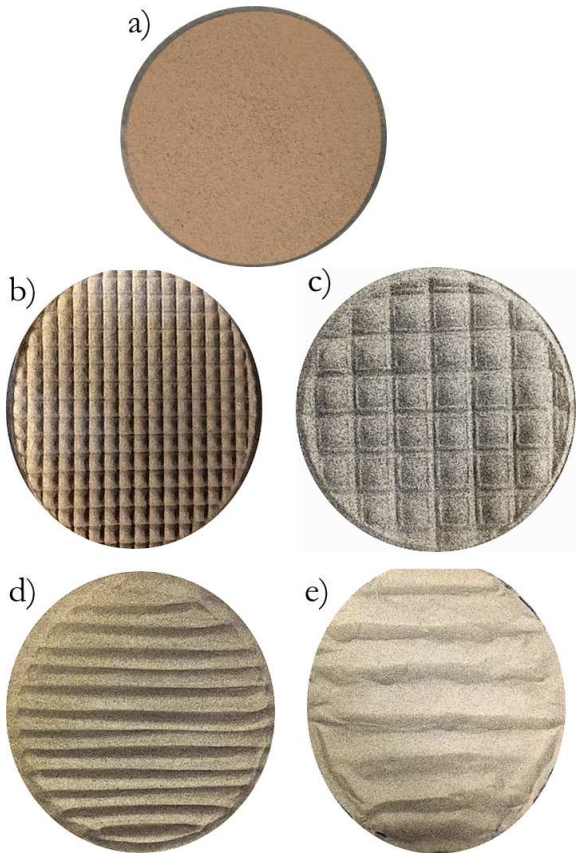

Fig. 1. The prepared samples used in this study: a) *S-Smooth*, b) *S-Grid10*, c) *S-Grid25*, d) *S-Wave10*, and e) *S-Wave25*.

D. Radiometric and Point Cloud Analysis

We obtained BCRF measurements of each of the previously discussed samples using an intensity controlled 300 Watt studio fresnel lamp oriented at two inclination angles along the principal plane: 25° and 55°. These two different orientations simulated solar illumination conditions and allowed us to empirically assess the photometric effect of macroscopic surface roughness under both oblique and nadir-like illumination angles. The 25° illumination direction mimics a solar geometry that would be observed during daytime conditions in the northern hemisphere, while the 55° illumination orientation is considered for illustrating effects of extreme shadowing. Illumination at 25° tends to produce more multiple scattering, while the more oblique illumination direction of 55°, produces more single scattering and less multiple scattering [26]. In addition, we obtained BCRF measurements of sample *S-Smooth* at a variety of illumination inclination angles in order to forward model the Hapke roughness correction.

The distance from the fore-optic to the top of the sample holder at nadir viewing was ∼55 cm, which results in a projected field-of-view (FOV) at the target plane of ∼18 cm^2, when using a 5° FOV attachment. The most extreme sampling zenith angle in this study was 65°, which results in a projected FOV onto the surface takes on an elliptical area of $\sim$ 42 cm^2. The sample holder was 25.4 cm in diameter, which

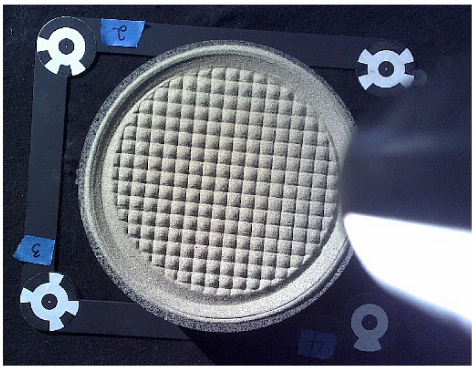

Fig. 2. An image obtained by GRIT-T's digital camera of sample *S-Grid10*. The ground control points are affixed to the corners of a rigid frame. The sensor fore-optic is also seen in the right-hand side of the image.

was sufficiently large to ensure that only sand surface facets influenced the spectral measurements. We used an irradiance meter with a cosine collector attachment to verify that the irradiance from the studio light source at the edges of this projected FOV area was constant to within 2%.

In the literature, there are studies of the impact of directionality of sand wave ridges relative to the principal plane on the BCRF. For this reason, we also measured BCRFs with the the ridges of samples *S-Wave10* and *S-Wave25* in three different orientations relative to the principal plane of the light source: parallel to the direction of the principal plane, perpendicular to the principal plane, and at a 45 degree angle to the principal plane. This allowed us to empirically assess the effect of directional shadowing on the BCRF of a rough sample.

We generated structure from motion point clouds for use in digital elevation calculations of the surfaces using the programming tools outlined in Section III-B. We outline in Section III-F how we used these point clouds to measure two different well-known roughness metrics from the surfaces of interest: the Hapke mean slope angle parameter and the random roughness metric.

E. Post-Processing SFM Point Clouds

As was mentioned in an earlier section, the size of objects within the scene must be known to the user in order to properly scale SfM point clouds [28]. To achieve this purpose, we used a custom built frame with ground control points printed on the corners to scale the point clouds. These targets have contrasting centers that are well-resolved by GRIT-T's on-board camera system at a nominal operating distance of 70 cm. We define the plane passing through the centers of these ground control points as the plane perpendicular to the $z-axis$. An example of an image obtained by GRIT-T's on-board camera system of sample *S-Grid10* is shown in Fig. 2.

We processed the output SFM point clouds from the $VisualSFM$ program using a custom processing chain. We first removed noisy points by using a sliding window filter over each point, $(x^{(i)}, y^{(i)}, z^{(i)})$. Within the window, we calculated the average elevation, $\bar{z}_{NN}$, and standard deviation, σ_{NN},

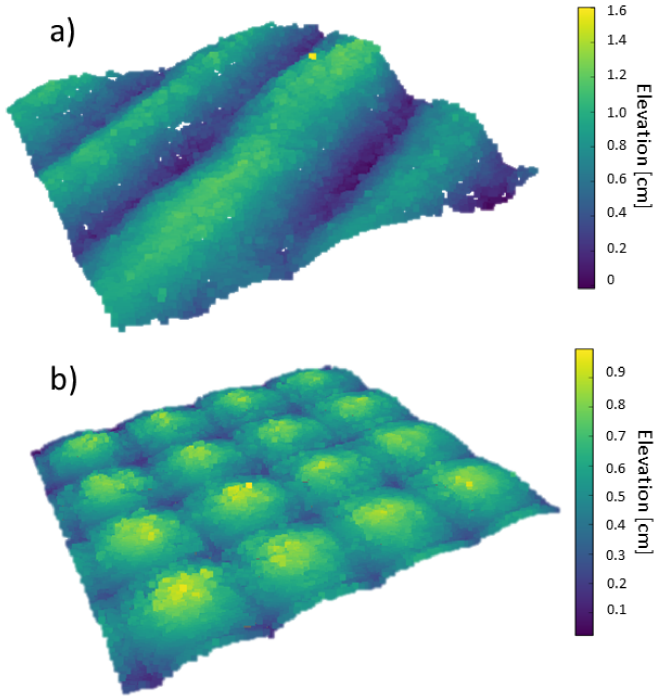

Fig. 3. Point clouds obtained using the post-processing scheme outlined in Section III-E: a) sample *S-Wave25*, and b) sample *S-Grid25*. The colorbar is relative to minimum elevation of the surface.

of the elevations of the point's N nearest neighbors on the basis of Euclidean distance. We marked any point satisfying $|z^{(i)} - \bar{z}_{NN}| > \alpha\sigma_{NN}$ as outliers, where α is a tuning parameter. Some examples of the resulting point clouds of this post-processing scheme are shown in Fig. 3.

We then performed a smoothing operation using a Delaunay triangulation on the output point cloud. We used a horizontal grid resolution $g = 0.25$ cm^2 to specify the grid's spatial sampling along the $x-$ and $y-axes$. A Delaunay triangulation is a triangulation of the convex hull of points within the point cloud [29]. The result is a linearly interpolated series of triangles defined by sets of vertices for each triangle. The surface normals of these triangular faces are used to calculate surface facet slope angles. An additional benefit of this step is the generation of a down-sampled version of the point cloud that is ideal for calculating roughness metrics.

F. Calculation of Hapke Mean Slope Angle Metric

The ultimate goal of our research is to relate experimental measurements to geophysical parameters through the inversion of Hapke's photometric model. In order to meet this end, we developed a routine to directly calculate the mean slope angle parameter, $\bar{\theta}$, from post-processed SfM point clouds. This parameter is used to forward model Hapke's correction for macroscopic roughness to the photometric model for a smooth surface, outlined in Section II-B [1].

We used the output millimeter scale triangular facets resulting from the Delaunay triangulation routine to calculate the slope angle relative to the $z-axis$ of each facet's surface normal. For samples *S-Grid10* and *S-Grid25*, we found that

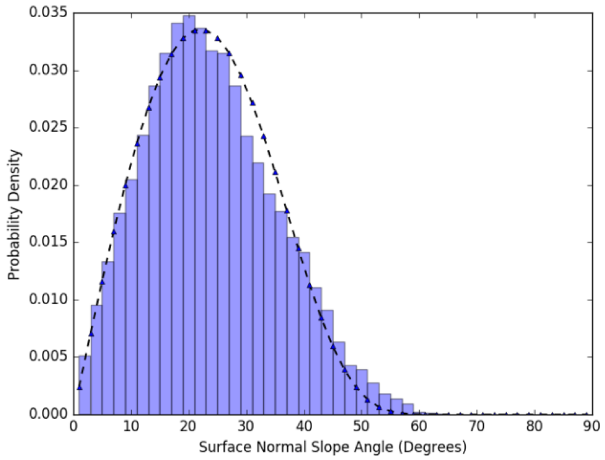

Fig. 4. Results of an optimal least-squares fit of the theoretical Hapke slope distribution, $a(\theta)$, (dotted line) to the empirically measured probability density function (histogram bars) for sand sample *S-Grid10*.

the azimuthal orientation of the facet surface normals showed no preference for direction, satisfying Hapke's criterion that the micro-facets of the surface should be randomly distributed azimuthally [1]. Despite the fact that the samples *S-Wave10* and *S-Wave25* exhibit strong preference for azimuth orientation, we also computed the optimal $\bar{\theta}$ metric for these samples for the sake of comparison.

In Hapke's model for macroscopic roughness, $a(\theta)$ (defined by (4) and (5)) is normalized over slope angles in the range $[0, \pi/2]$. We generated a normalized histogram of the facet slope angles to approximate the slope angle probability density function (PDF), with bins spanning every 2°. We then calculated $a(\theta)$ using the PDF resulting from the binning process. We performed a least squares regression of the function $a(\theta)$ to optimally fit the mean slope angle parameter to the resulting PDF on the basis of a percentage difference error metric. We show an example of an optimal fit of slope distribution $a(\theta)$ to the empirically measured PDF of sample *S-Grid10* in Figure 4.

G. Elevation Roughness Metrics

We also calculated a simple Random Roughness (RR) metric from the post-processed SfM point clouds. The RR metric is frequently used as a baseline measure in many studies of soil roughness [30]. The metric is defined in (13):

$$RR = \sqrt{\frac{1}{N}\sum_{i=1}^{N}(z^{(i)} - \bar{Z})^2} \tag{13}$$

where N is the total number of surface facet measurements obtained, $z^{(i)}$ is the elevation of the i^{th} surface facet center, and $\bar{Z}$ is mean elevation of all surface facet centers. Some disadvantages of the RR metric are that it does not take into account horizontal information regarding macroscopic roughness, and that it is not derived from any specific physical model [31].

Additionally, we calculated another well-known roughness metric used in the agricultural community known as the height standard deviation (HSD) of the surface. This was calculated using the definitions outlined in [21], and calculated for all samples used in this study.

H. Retrieved Roughness Metrics

We calculated the mean slope angle roughness metric and the random roughness metric for each roughness state using the previously derived roughness metric definitions. We show the retrieved metrics for each roughness state in Table I. One

TABLE I
THE RETRIEVED METRICS DERIVED FROM THE RANDOM ROUGHNESS (RR) METRIC CALCULATION, THE HSD CALCULATION, AND THE OPTIMAL PHOTOMETRIC MEAN SLOPE ANGLE ($\bar{\theta}$) FIT.

Sample	Grid Interval	RR (cm)	HSD (cm)	$\bar{\theta}$ (degrees)
S-Smooth	0 mm	0.001	0.001	0.015
S-Wave10	10 mm	0.109	0.081	16.75
S-Wave25	25 mm	0.265	0.21	20.34
S-Grid10	10 mm	0.102	0.085	16.84
S-Grid25	25 mm	0.137	0.121	14.20

of our goals was to isolate the photometric effect of surface roughness but also to maintain a constant density across all samples. In Table I we observe that the derived mean slope angle values, $\bar{\theta}$ which resulted from a least squares fit of the facetized surface slope angle distribution to the Hapke slope distribution, $a(\theta)$, are similar across all roughness states used in this study. In addition, the derived RR metrics are similar across all samples, with the exception of sample *S-Wave25*, which was created by using a grid spacing with a 25 mm separation.

We assume that the grain size distribution and surface density remained approximately constant across all samples. As a result of this, maintaining approximately constant roughness metric values across all roughness states allowed us to directly compare the photometric effect of azimuthally oriented roughness ($wave-like$) to the photometric effect of azimuthally random roughness ($grid-like$). Hapke predicts that differences in the photometric effect of macroscopic surface roughness can be solely determined by the distribution of the facetized slopes of a surface [1]. Therefore, we hypothesized that because the facet slopes of samples *S-Grid10* and *S-Grid25* are not distributed with azimuthal preference, that the photometric effect of the macroscopic surface roughness of these samples should be equivalent despite the fact that the surface roughness of sample *S-Grid10* is of a higher spatial frequency than the surface roughness of sample *S-Grid25*.

I. Empirical Forward Modeling of Hapke Roughness Correction Factor

One of our stated goals was to assess how well Hapke's correction for macroscopic surface roughness is able to compensate for experimentally observed effects of photometric surface roughness. In order to perform this analysis, we needed to estimate the parameter $\bar{\theta}$ derived by Hapke [1]. We assumed accurate estimation of $\bar{\theta}$, defined in (3), since the estimates

were based on digital point clouds accurate in horizontal resolution to within 0.10 cm. After $\bar{\theta}$ had been estimated for the surface profile of interest, the effective incident zenith angle i_e could be calculated. The value of i_e tells us the effective incident light zenith angle of the smooth sample BCRF that is needed to empirically forward model the roughness correction factor.

The proper calculation of the correction factor in (6) requires knowledge of the reflectance into an effective viewing zenith angle e_e from a smooth surface due to incident radiation from an effective incident zenith angle i_e. One method for determining the reflectance from a smooth photometric model at these effective zenith angles requires performing full model inversion for all parameters of the photometric model for a smooth sediment surface. This method is quite difficult due to the many parameters in (1) creating the possibility of getting stuck in local minima while performing model inversion [14], [26]. Our proposed novel method for obtaining $r(i_e, e_e, g)$ is to calculate i_e using (7) and (10) and the $\bar{\theta}$ values from Table I. This method allows us to empirically forward model the correction factor in (6).

We calculated the effective incident angles i_e for all viewing orientations of the measured experimental rough surface BCRFs in this study at the incident light zenith angles of 25° and 55° by using (7) and (10). Statistics of the retrieved values of i_e from these calculations appear in Table II. We only performed these operations for samples *S-Grid10* and *S-Grid25* because these met Hapke's criterion that there should be no azimuthal preference for the direction of facet slope normal angles [7].

Using GRIT-T, we measured BCRFs of sample *S-Smooth* at a high directional sampling density (azimuth intervals of 10° and zenith intervals of 10°) for the values of $Median\ i_e$ in Table II. The sampled zenith range was from 0-65° and the sampled azimuth range was from 0-360°. In order to account for the range of values of i_e that can result from (7) and (10), we only considered directionally sampled points at viewing orientations (e_e, ψ) if the corresponding i_e value was within the range of $Median\ i_e \pm 1.0°$.

Using this process, we obtained a BCRF of a smooth surface, $r(i_e, e_e, g, \omega)$, that with the application of the shadowing function $S(i, e, g)$ correction function should yield the BCRF of a rough sample, $r_r(i, e, g, \omega, \bar{\theta})$, defined by mean slope angle $\bar{\theta}$. Calculation of the shadowing function $S(i, e, g)$ in (12) and (9) allows us to experimentally forward propagate Hapke's roughness correction factor in (6). To differentiate these two different variables, we denote the forward modeled BCRF for a rough surface by the name $r_{modeled}(i, e, g, \omega, \bar{\theta})$ and the corresponding measured BCRF for a rough surface as $r_{measured}(i, e, g, \omega, \bar{\theta})$.

IV. Results and Discussion

A. Comparison of Normally Distributed Roughness with Oriented Roughness

Under the assumption that the density of the sample *S-Smooth* is approximately the same as the density of the rough surface samples, we are able to directly compare the resultant

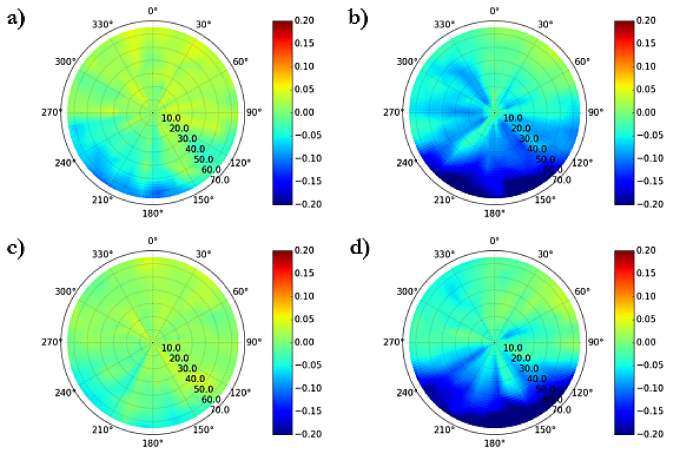

Fig. 5. Plots of $\Delta\%_{rough}(e, \phi)$ for light illumination $i = 25°$ at wavelength $\lambda = 650$ nm. The images correspond to the following samples: (a) *S-Grid10*, (b) *S-Wave10* with surface waves oriented perpendicular to the principal plane, (c) *S-Grid25*, and (d) *S-Wave25* with surface waves oriented perpendicular to the principal plane.

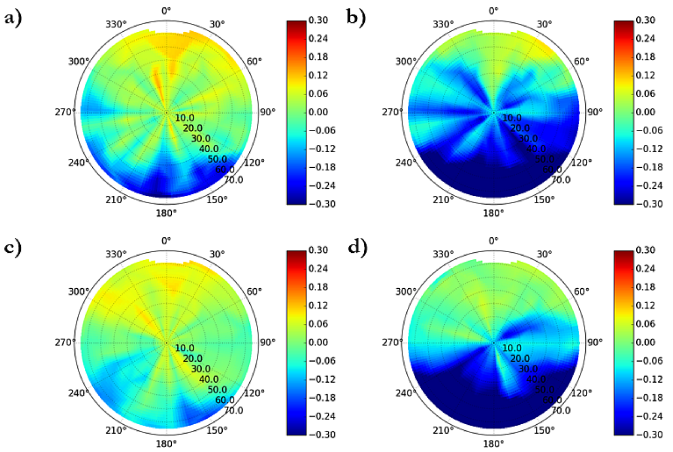

Fig. 6. Plots of $\Delta\%_{rough}(e, \phi)$ for light illumination $i = 55°$ at wavelength $\lambda = 650$ nm. The images correspond to the following samples: (a) *S-Grid10*, (b) *S-Wave10* with surface waves oriented perpendicular to the principal plane, (c) *S-Grid25*, and (d) *S-Wave25* with surface waves oriented perpendicular to the principal plane.

BCRFs and isolate the photometric effects of macroscopic surface roughness. We begin by comparing the empirical BCRF measurements for smooth and rough surfaces for the different types of roughness previously described. We used a percentage difference metric of the change in BCRF magnitude of a rough sample, r_{rough}, relative to BCRF magnitude of a smooth sample, r_{smooth}, in order to characterize differences as a function of sensor viewing orientation. The metric $\Delta\%_{rough}(e, \phi, \lambda)$ provides insight into the photometric effect of roughness based on the fact that Hapke's shadowing correction factor is a multiplicative factor that is applied to a smooth surface reflectance [1].

$$\Delta\%_{rough}(e, \phi, \lambda) = \frac{r_{rough}(e, \phi, \lambda) - r_{smooth}(e, \phi, \lambda)}{r_{smooth}(e, \phi, \lambda)} \quad (14)$$

TABLE II
STATISTICS CALCULATED FOR i_e FOR THE SAMPLES USED IN THIS STUDY. THE RANGE OF THE VALUES OF i_e VARIES BASED ON THE INCIDENT ZENITH ANGLE (i), THE EMERGENT ZENITH ANGLE (e), AND THE MEAN SLOPE ANGLE ($\bar{\theta}$) OF THE SURFACE ROUGHNESS.

Sample	i (degrees)	$\bar{\theta}$ (degrees)	Median i_e	Std. Dev. i_e	Minimum i_e	Maximum i_e
S-Grid10	25	16.84	37.0	0.72	36.9	40.0
	55	16.84	58.4	0.95	57.15	62.6
S-Grid25	25	14.20	34.2	0.44	34.2	36.2
	55	14.20	58.2	0.55	57.6	60.5

The results of performing this operation at a wavelength $\lambda = 650$ nm for incident illumination conditions of $i = 25°$ are shown in Fig. 5. We note that we performed this portion of the analysis using the BCRF measurements of *S-Wave10* and *S-Wave25* for the case where the wave surface was oriented perpendicular to the incident illumination direction. We observe that samples *S-Wave10* and *S-Wave25* exhibit a greater reduction in forward scattered reflectance than samples *S-Grid10* and *S-Grid25*. This observation suggests that the wave-like roughness profiles had a greater impact on forward scattered reflectance than the grid-like roughness. One reason for this behavior is likely that the surface waves reduce specular reflectance due to the higher proportion of surface area with vertical slopes; this leads to an increased proportion of shadowed surface area.

We also examined the results obtained when calculating $\Delta\%_{rough}(e, \phi)$ when the light was oriented at an oblique zenith angle of $i = 55°$ for a wavelength $\lambda = 650$ nm. We plot these results in Fig. 6. We once again observe that samples *S-Wave10* and *S-Wave25* exhibited a greater reduction in forward scattered reflectance than samples *S-Grid10* and *S-Grid25*. We also note that there is a larger decrease in forward scattered reflectance than for the case of $i = 25°$. This can be expected based on a simple geometric ray tracing argument that has been demonstrated in previous studies. We expect a larger proportion of the surface area of cavities of the surface waves to be in shadow in the case of the source illumination being at larger zenith angle value [32]. While we only show results for a wavelength $\lambda = 650$ nm, we found that these results were consistent across the entire spectral domain from 350 nm to 2500 nm.

B. Observed Ability to Discern Directional Shadowing

There have been few studies that attempt to examine the effect that directional roughness has on the BCRF of a sediment surface. Many models, including those developed by [3] and [1], attempt to model roughness as being randomly distributed in azimuthal facet orientation.

We examined directional reflectance measurements of samples *S-Wave10* and *S-Wave25* under cases cases where the surface waves were oriented in three different azimuthal orientations relative to the principal plane of incident illumination, the azimuth arc from $\psi = 0°$ to $\psi = 180°$. These orientations for the surface waves were: (1) perpendicular to the principal plane, (2) rotated 45 degree clockwise relative to the principal plane, and (3) parallel to the principal plane. Results obtained for sample *S-Wave10* when the illumination source was oriented at $i = 25°$ and $i = 55°$ are shown in Fig. 7 for a wavelength $\lambda = 650$ nm.

Fig. 7 (b) and (e) are an interesting case when the surface waves are rotated 45° clockwise relative to the principal plane. We easily see that the shadows being cast over an azimuthal extent from $\psi = 120°$ to $\psi = 180°$ appear as a local minimum in reflectance. In addition, we observe in Fig. 7 (b) that when the light source is at $i = 25°$ there is an increase in forward scattered reflectance over the range $\psi = 180°$ to $\psi = 240°$, when compared with the ridges that are oriented perpendicular to the illumination principal plane. This observation can potentially be explained by inter-facet multiple scattering. Hapke has noted that inter-facet multiple scattering of light fills cavities and can lead to a 6% increase in reflectance for sediment surfaces with single scattering albedos of 0.5 and a maximum facet slope angle of $0.45°$ [1]. In addition, [33] argued that the phenomenon of inter-facet multiple scattering causes the photometric effects of shadowing to effectively become negligible for macroscopically rough surfaces.

In Fig. 7 (c) and (f) we show results from BCRF measurements where the surface waves of *S-Wave10* are oriented parallel to the principal plane for $i = 25°$ and $i = 55°$, respectively. It is also evident that the large backscatter lobe that is similar to the case where the ridges were oriented perpendicular to the direction of incident illumination. We also see the appearance of a forward scattering lobe in the azimuth range of $\psi = 150°$ to $\psi = 210°$ at extreme sensor zenith orientations of $e = 40°$ to $e = 65°$ that represents a large increase in specularly scattered radiance. We also observe that for azimuth orientations that are further offset from the principal plane there is a local minimum in reflectance. This is seen at azimuth orientations of $\psi = 90°$ and $\psi = 270°$ for extreme sensor zenith angles.

One reason for this phenomenon could be that for sensor orientations that are offset from the principal plane by an absolute azimuth value of ± 90 degrees the troughs of the surface cavities are partially hidden from the field-of-view of the sensor by the peaks of the surface waves. This idea is suggested by Hapke [1] when deriving the correction shown in (6). In his derivation, Hapke [1] defined different correction factors for two cases of sun-sensor geometries: one for the case when incident illumination zenith angle is less than the sensor's zenith angle, and another for the case where the sensor zenith angle is greater than the illumination zenith angle. Additionally, Clavano [32] notes that simulation environments for modeling the photometric effects of roughness must take into account the effects of surface crests blocking incident light from reaching troughs of cavities, and the effects of crests blocking the sensor from viewing the bottom of surface cavities. The results shown here indicate support these conclusions for cases where waves of a roughness profile are

oriented parallel to the principal plane of incident radiation.

The results shown in Fig. 7 exhibit clear experimental evidence that can be used in developing photometric correction factors for the case of surface roughness that is not randomly distributed in azimuthal orientation of microfacets.

C. Forward Modeling of Hapke Roughness Correction

We used the steps outlined in Section III-I to calculate $r_{modeled}(i,e,g,\omega,\bar{\theta})$ for all of the samples in this study. We used the $\bar{\theta}$ values shown in Table I to accomplish this. In Fig. 8, we compare the forward-model result $r_{modeled}(i,e,g,\omega,\bar{\theta})$ to that obtained by direct measurement from a rough surface, $r_{measured}(i,e,g,\omega,\bar{\theta})$, for an example wavelength of λ =650 nm. The first column of Fig. 8 shows the measured BCRF of a smooth sample, $r(i_e,e_e,g,\omega)$, at $\lambda = 650$ nm using an illumination zenith angle corresponding to the ***Median*** i_e value from Table II. The second column shows the wavelength-independent shadowing function $S(i,e,g,\bar{\theta})$ computed for the roughness level of the sample. The third column shows the forward modeled reflectance of the sample, $r_{modeled}(i,e,g,\omega,\bar{\theta})$, which is the product obtained by multiplying the values from the first two columns, i.e. using (6). The fourth column is the corresponding empirically measured BCRF, $r_{measured}(i,e,g,\omega,\bar{\theta})$, for the rough sample. The rows of Fig. 8 portray these steps of the forward-modeling and comparison to the BCRF measured directly for each of the four rough surfaces *S-Grid10*, *S-Grid25*, *S-Grid10*, and *S-Grid25*.

We observe many differences between $r_{measured}(i,e,g,\omega,\bar{\theta})$ and $r_{modeled}(i,e,g,\omega,\bar{\theta})$ for all of the samples. The form of $r_{modeled}(i,e,g,\omega,\bar{\theta})$ is probably strongly influenced by volumetric scattering from the smooth sample BCRF in (6), which causes a "bowl shape" due to a local maximum in reflectance at large sensor viewing zenith orientations [7]. As Fig. 8 demonstrates the form of the Shadowing Function $S(i,e,g,\bar{\theta})$ leads to a $r_{modeled}(i,e,g,\omega,\bar{\theta})$ that does depart from the observed rough surface result $r_{measured}(i,e,g,\omega,\bar{\theta})$ in a couple of important ways. The polar plots of $r_{modeled}(i,e,g,\omega,\bar{\theta})$ show that the major differences occur at extreme sensor zenith orientations of $e \geq 40°$. In the extreme forward scattering direction the plots of $r_{modeled}(i,e,g,\omega,\bar{\theta})$ have a local maximum that is not present in the plots of $r_{measured}(i,e,g,\omega,\bar{\theta})$. In addition, $r_{modeled}(i,e,g,\omega,\bar{\theta})$ also has a substantial and broad local minimum centered close to $e = 0°$; however, this broad minimum does not appear in $r_{measured}(i,e,g,\omega,\bar{\theta})$.

In order to quantitatively analyze the differences between $r_{measured}(i,e,g,\omega,\bar{\theta})$ and $r_{modeled}(i,e,g,\omega,\bar{\theta})$, we computed a percentage difference defined by:

$$\Delta\%(i,e,g,\bar{\theta_i},\lambda) = 100\frac{r_{measured}(i,e,g,\bar{\theta_i},\lambda) - r_{modeled}(i,e,g,\bar{\theta_i},\lambda)}{r_{measured}(i,e,g,\bar{\theta_i},\lambda)} \quad (15)$$

Fig. 9 shows the results of calculing (15) for the samples used in this study for the example wavelength $\lambda = 650\,nm$. From these plots, we observe that the largest values of $\Delta\%$ occur at extreme viewing zenith orientations in the forward scattering direction. For nadir-like illumination conditions of $i = 25°$, $r_{modeled}(i,e,g,\omega,\bar{\theta})$ exceeds the experimentally measured directional reflectance by approximately 20%. For oblique illumination conditions $i = 55°$, $r_{modeled}(i,e,g,\omega,\bar{\theta})$ exceeds the experimentally observed directional reflectance by up to 45%. These results suggest that (6) underestimates the role that shadows cast by surface waves have on the forward scattered reflectance of sand sediments.

The underlying cause of the differences of the results seen in Fig. 9 likely depends on the observed behavior of the shadowing function defined by (9) and (12) for different illumination angles. Fig. 8, shows that the shadowing function is approximately equal to 1.0 for the BCRFs obtained using illumination conditions $i = 25°$. It can also be seen that for oblique illumination conditions $i = 55°$, the shadowing function only predicts a slight decrease of 4-8% in forward scattered reflectance at extreme viewing zenith angles $e = 60°$. In Fig. 10, we illustrate the behavior of the shadowing function for the roughness level of *S-Grid25*, with $\bar{\theta} = 14.20°$, in three-dimensional polar renderings over a wider range of illumination angles. This Figure illustrates that the shadowing function does not have a strong impact on the forward scattered reflectance until much larger view zenith angles are reached: only cases c) and d) at respectively i = 70° and i = 85° show a substantial change in this multiplicative factor in the forward scattering direction.

The polar renderings are plotted with a colorbar that indicates the magnitude of the shadowing function. A value of $S(i,e,g) = 1$ takes on a reddish hue and signifies that macroscopic surface roughness does not have a photometric effect at this viewing orientation. A value of $S(i,e,g) = 0$ takes on a purple hue and indicates that macrosopic roughness completely shadows this viewing orientation. The polar renderings are plotted over a viewing zenith range of $e \in [0°, 90°]$ across the entire azimuth range of the hemisphere. For example, a coordinate of ($x = 1$, $y = 0$) in these polar renderings corresponds to ($e = 90°$, $\psi = 0°$), where ψ represents the viewing azimuth angle. The principal plane lies along the line $y = 0$.

These renderings show that Hapke predicts that shadowing has little photometric effect on directional reflectance when the surface is illuminated by light at an incident zenith angle in the range of $i \in [25°, 55°]$. Even at extreme viewing geometries of $e = 90°$ the shadowing function for $i = 55°$ is approximately equal to 1.0 for all viewing orientations. Only when the light is oriented at extreme illumination zenith angles of $i \geq 70°$ does shadowing begin to drastically affect the directional reflectance. For these scenarios, we observe that Hapke predicts a steep drop in forward scattered reflectance [7]. These results do not match the observed photometric effect of shadowing seen in our results.

Since the shadowing function is by definition (Equations (9) and (12)) independent of wavelength, our analysis focused on the angular dependence of $S(i,e,g) = 1$. As we have seen, $S(i,e,g) = 1$ overestimates the amount of forward scattering and the extent and shape of a local minimum in reflectance near nadir. To more completely understand differences between the model and observations, we examined the dependence of the photometric effect of shadowing on the relative orientation of the sensor to the viewing direction. To accomplish this, we used the definition of phase angle, g [7],

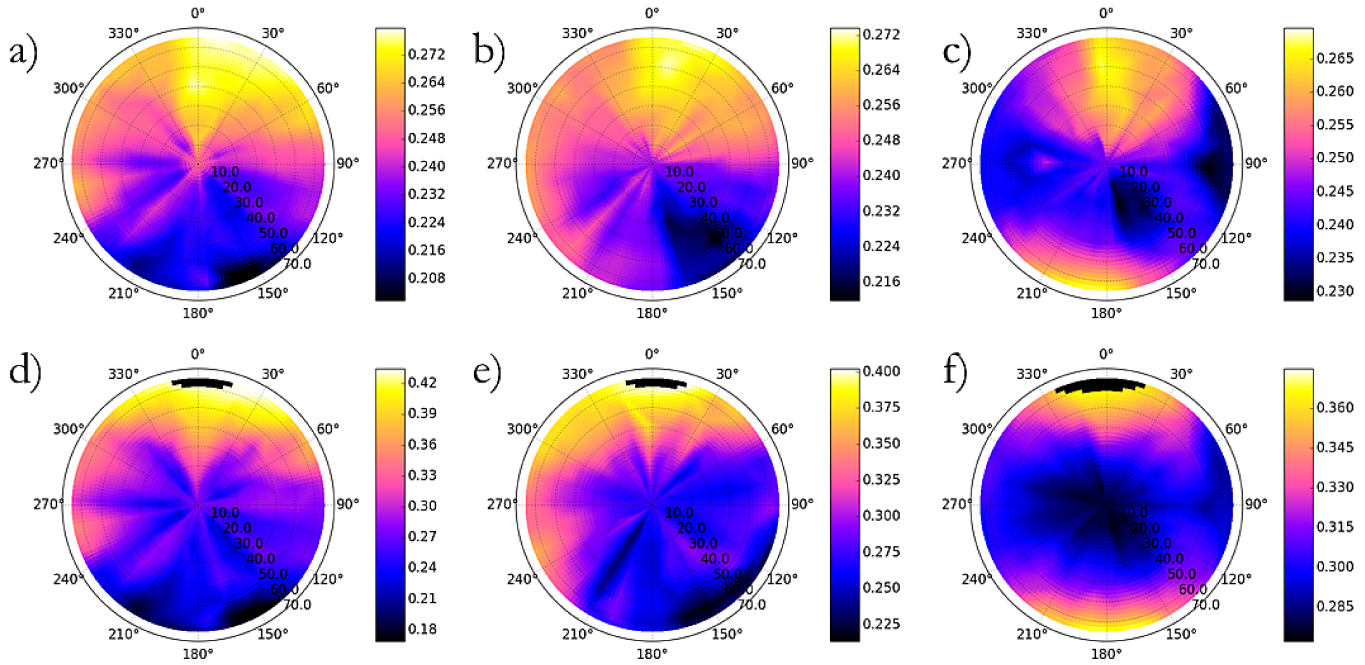

Fig. 7. Rendering of BCRF measurements at a wavelength $\lambda = 650$ nm for sample *S-Wave10* with directionally oriented surface waves. The top row shows BCRF measurements obtained with illumination $i = 25°$ and the bottom row shows BCRF measurements obtained with $i = 55°$. The images correspond to the following samples: (a, d) *S-Wave10* with surface waves oriented perpendicular to the principal plane (b, e) *S-Wave10* with surface waves oriented at a $45°$ angle clockwise related to the principal plane, (c, f) *S-Wave10* with surface waves oriented parallel to the principal plane. In these plots, the azimuth direction of $0°$ denotes the solar illumination direction.

which depends on both the sensor viewing geometry and the illumination geometry:

$$g = \cos^{-1}\left(\cos i \, \cos e + \sin i \, \sin e \sin \psi\right) \tag{16}$$

We averaged results for the percentage difference $\Delta\%(i, e, g, \bar{\theta_i}, \lambda)$ defined in (15) for the following sensor orientation phase angles: $10°$, $30°$, $45°$, $65°$, $80°$, and $100°$. These values represent a broad range of phase angles where at least 5 viewing orientation points could be averaged at a given phase angle. Fig. 11 shows the results for *S-Grid25*. These plots suggest that at larger phase angles ($g \geq 65$), the percentage difference between modeled and measured reflectance exhibits some spectral dependence, primarily in the shorter wavelength end of the spectral range measured by GRIT-T, where we observe a monotonic increase with wavelength. However, between $1000 - 1800\,nm$, our results do not exhibit a strong wavelength dependence. Between $2000 - 2500\,nm$, the results are also relatively independent of wavelength, but there is a difference in error level compared with the $1000 - 1800\,nm$ spectral region overall.

V. Conclusion

We analyzed the photometric effects of both "grid-like" and "wave-like" roughness profiles of sand samples in a controlled laboratory setting for illumination at oblique zenith angles as well as close to nadir. The "grid-like" roughness samples satisfied Hapke's criterion for his derived correction factor that a surface's roughness should be distributed uniformly in azimuth [1], while the "wave-like" samples represented surface profiles that do not meet Hapke's underlying assumptions. All of the different roughness samples were prepared using a geotechnical protocol for manipulating the roughness of a sand surface while holding the sediment density (using an ASTM standard) and grain size distribution approximately constant, allowing us to isolate the photometric effects of roughness.

A major goal of the study was to compare experimentally observed BCRF measurements of a rough sediment surface to forward-modeled BCRF measurements by incorporating an empirically derived estimate of roughness from a DEM into Hapke's photometric correction for macroscopic roughness. The proper calculation of the correction factor in Hapke's photometric model for a rough surface requires knowledge of the reflectance into an effective viewing zenith angle e_e from a smooth surface due to incident radiation from an effective incident zenith angle i_e. Due to the large number of freely varying parameters in Hapke's photometric model, there is a large probability of getting stuck in local minima while performing model inversion [14], [26]. Rather than perform this full model inversion, we chose to experimentally obtain the parameter i_e from roughness metrics of rough samples at a sub-centimeter scale. This method allowed us to forward-model the correction factor from an empirically derived measure of roughness $\bar{theta}$, thereby circumventing the need to perform model inversion, and allowing a direct test of model consistency.

The results of comparing forward-modeled results to experimental results indicate that Hapke's correction factor does not adequately account for the photometric effects of sub-centimeter surface roughness. By modeling the shadowing function of Hapke's correction factor, we observed that Hapke

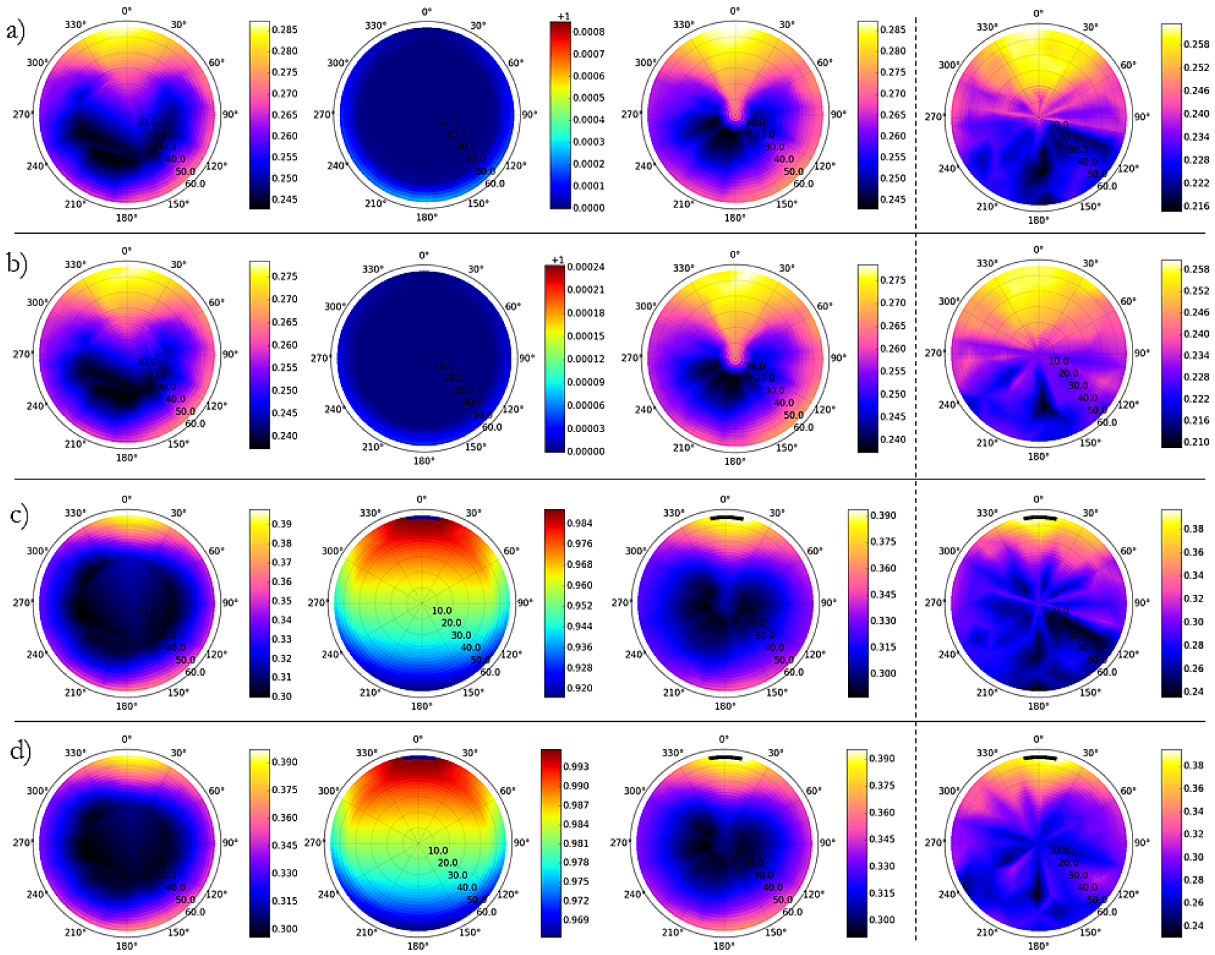

Fig. 8. Empirical forward modeling of (6) for spectral BCRF measurements obtained at 650 nm. Results are shown for a) sample *S-Grid10* with $i = 25°$, b) sample *S-Grid25* with $i = 25°$, c) sample *S-Grid10* with $i = 55°$, and d) sample *S-Grid25* with $i = 55°$. The first column shows $r(i_e, e_e, g)$ obtained using light illumination of $Median\, i_e$ from Table II. The second column shows the shadowing function $S(i, e, g, \bar{\theta})$ using the $\bar{\theta}$ values from Table I. The third column shows the forward modeled directional reflectance for a surface with $\bar{\theta}$ obtained by multiplication of columns 1 and 2. The fourth column shows the corresponding empirically measured BCRF for the sample at 650 nm. In these plots, the azimuth direction of 0° denotes the solar illumination direction.

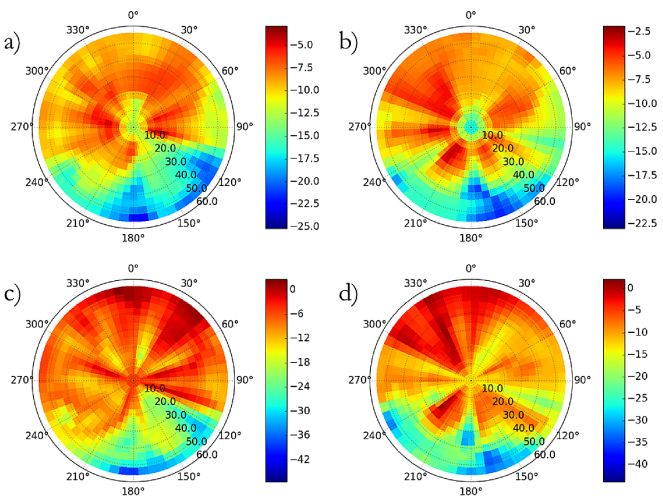

Fig. 9. Percent difference plots between forward modeled and empirically measured BCRFs at 650 nm for a) *S-Grid10* with $i = 25°$, b) *S-Grid25* with $i = 25°$, c) *S-Grid10* with $i = 55°$, and d) *S-Grid25* with $i = 55°$.

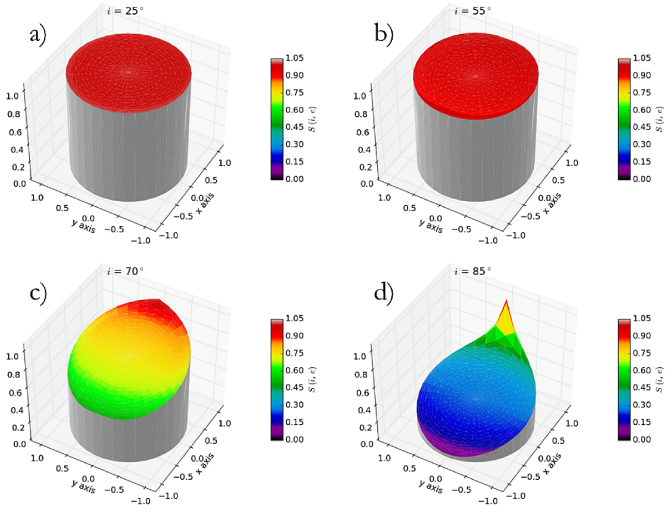

Fig. 10. Polar renderings of the shadowing function $S(i, e, g, \bar{\theta})$ for roughness level of $\bar{\theta} = 14.20°$ for varying illumination conditions of i: a) 25°, b) 55°, c) 70°, and d) 85°.

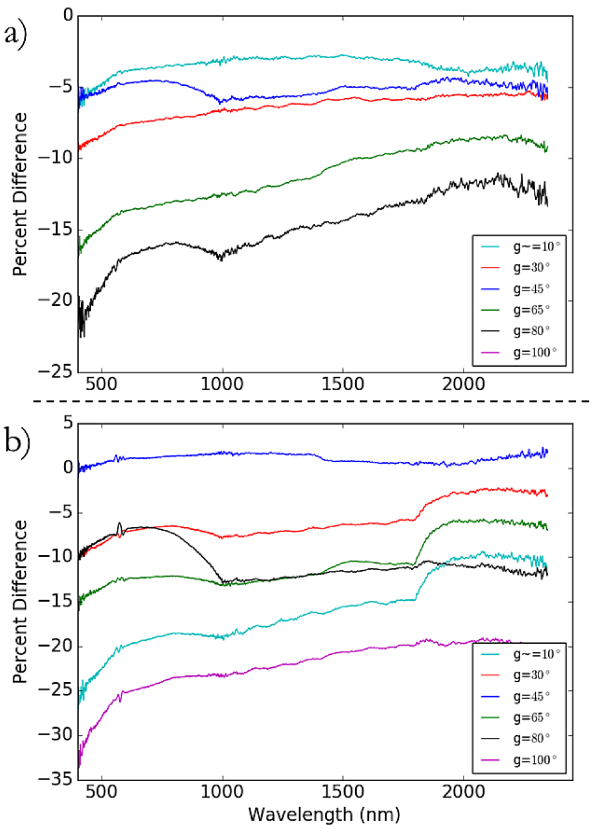

Fig. 11. Percent difference plots between forward modeled and empirically measured BCRFs for selected phase angles as a function of wavelength for a) *S-Grid10* with i = 25°, b) *S-Grid25* with i = 55°.

predicts a steep drop in forward scattered reflectance only at extreme illumination zenith angles of $\geq$ 70°. We also determined that there was an approximately constant percentage difference between the forward modeled and experimentally observed BCRF measurements across wavelengths (except at small wavelengths), which provides evidence that the shadowing function can potentially be corrected to match experimental results.

It should be noted that the scale over which the photometric mean slope angle is valid is subject to debate. Hapke originally assumed that the macroscopic surface roughness, and therefore the amount of shadowing that occurs on the surface, occurred at all scales ranging from the size of an individual grain, all the way up to the range of kilometer scale sensors [1]. However, Hapke later suggested that the surface reflectance would be dominated by the largest slope magnitude values, which occur on the order of individual grains due to the fact that at this range particle cohesiveness dominates over gravity [7]. In another study, Shepard and Campbell [33] modeled the shadowing behavior of fractal surfaces by using computer simulated planetary surfaces. Their study results suggested that the scale of roughness that dominates photometric effects of roughness is the smallest extent at which shadows still exist. They argued that processes such as multiple scattering between facets of the surface cavities and the diffraction of light around individual grains remove the photometric effect of shadows below some measurable scale. They argue that these factors lead to a negligible contribution from extremely small scale shadows [33]. The aforementioned studies suggest that studying the effect of shadowing due to roughness on a millimeter to centimeter scale level should be sufficient to characterize the effect that inter-facet multiple scattering has on the BCRF of a sediment as a function of illumination zenith angle, but that the most important scale may be at a smaller scale than that considered by our digital elevation models.

We also compared the photometric effect of "grid-like" roughness samples with "wave-like" roughness samples. In this experiment, the samples were held at approximately constant density and therefore the photometric effect of roughness was isolated in the BCRF measurements. We observed that the BCRFs of the "wave-like" roughness samples had a significant reduction in forward scattered reflectance relative to the BCRFs of the "grid-like" roughness samples. We observed that surface waves tended to reduce specular reflectance. The higher proportion of surface area with steeper slopes may explain this observation because the presence of these steeper slopes leads to an increased proportion of shadowed surface area. This result indicates that a new shadowing function should be derived for the case of "wave-like" roughness conditions.

A final goal of our study was to assess experimentally the effects of orienting the surface waves of the "wave-like" roughness samples in different orientations relative to the principal plane. Our results provide experimental evidence that multiple scattering within the surface cavities reduces the effects of shadowing. This phenomenon was described by Shepard based on his experiments related to planetary sediments [33]. Our results provide experimental evidence for the same conclusion. In the future, these results can be used to develop photometric correction factors for the case of roughness that is characterized by surface waves oriented at different directions relative to incident illumination.

APPENDIX A
HAPKE ROUGHNESS CORRECTION PARAMETERS

In the process of deriving the correction factor, Hapke defined many variables that must be calculated in order to properly forward-model the rough surface photometric model. These ancillary factors that Hapke uses in the correction factor (6)[1] are defined as follow:

$$f(\psi) = \exp(-2\tan\frac{\psi}{2}) \tag{17}$$

$$\chi(\bar{\theta}) = 1/(1+\pi\tan\bar{\theta}^2)^{1/2} \tag{18}$$

$$E_1(y) = \exp(-\frac{2}{\pi}\cot\bar{\theta}\cot y) \tag{19}$$

$$E_2(y) = \exp(-\frac{1}{\pi}\cot^2\bar{\theta}\cot^2 y) \tag{20}$$

$$\eta(y) = \chi(\bar{\theta})[\cos y + \sin y\tan\bar{\theta}\frac{E_2(y)}{2-E_1(y)}] \tag{21}$$

In the equations above, the variable y can be used interchangeably to represent either the incident or emergent zenith angle of light from the sediment medium.

ACKNOWLEDGMENT

This research is funded by an academic grant from the National Geospatial-Intelligence Agency (Award No. #HM0476-17-1-2001, Project Title: Hyperspectral Video Imaging and Mapping of Littoral Conditions), Approved for public release, 19-084.

REFERENCES

[1] B. Hapke, "Bidirectional reflectance spectroscopy. 3. Correction for macroscopic roughness," *Icarus*, vol. 59, no. 1, pp. 41–59, 1984.
[2] R. L. Cook and K. E. Torrance, "A reflectance model for computer graphics," *ACM SIGGRAPH Computer Graphics*, vol. 15, no. 3, pp. 307–316, 1981. [Online]. Available: http://portal.acm.org/citation.cfm?doid=965161.806819
[3] J. Cierniewski and A. Marlewski, "Model for inferring soil surface roughness from soil directional reflectance data." in *17th EARSeL Symposium on Future trends in remote sensing*, 1998, p. 90.
[4] J. Cierniewski, T. Gdala, and A. Karnieli, "A hemispherical-directional reflectance model as a tool for understanding image distinctions between cultivated and uncultivated bare surfaces," *Remote Sensing of Environment*, vol. 90, no. 4, pp. 505–523, 2004.
[5] J. Cierniewski and M. Verbrugghe, "Influence of soil surface roughness on soil bidirectional reflectance," *International Journal of Remote Sensing*, vol. 18, no. 6, pp. 1277–1288, 1997.
[6] P. Beckmann, "Shadowing of random rough surfaces," *IEEE Transactions on Antennas and Propagation*, vol. 13, no. 3, pp. 384–388, 1965. [Online]. Available: http://ieeexplore.ieee.org/lpdocs/epic03/wrapper.htm?arnumber=1138443
[7] B. Hapke, *Theory of Reflectance and Emittance Spectroscopy*. Cambridge University Press, 2012.
[8] R. A. Bagnold, "The Physics of Blown Sand and Desert Dunes," *Nature*, vol. 148, pp. 480–481, 1941.
[9] E. Rehman, A. Gerace, M. Montanaro, B. Ambeau, and J. McCorkel, "Development of a simulation environment to support intercalibration studies over the Algodones Dunes system," *Journal of Applied Remote Sensing (JARS)*, vol. 12, no. 1, 2018. [Online]. Available: http://dx.doi.org/10.1117/1.JRS.12.012008
[10] Y. M. Govaerts, "Sand dune ridge alignment effects on surface BRF over the Libya-4 CEOS calibration site," *Sensors (Switzerland)*, vol. 15, no. 2, pp. 3453–3470, 2015.
[11] C. Bachmann, R. Eon, C. Lapszynski, G. Badura, A. Vodacek, M. Hoffman, D. Mckeown, R. Kremens, M. Richardson, T. Bauch *et al.*, "A low-rate video approach to hyperspectral imaging of dynamic scenes," *Journal of Imaging*, vol. 5, no. 1, p. 6, 2019.
[12] M. K. Shepard and P. Helfenstein, "A test of the Hapke photometric model," *Journal of Geophysical Research E: Planets*, vol. 112, no. 3, pp. 1–17, 2007.
[13] S. Labarre, C. Ferrari, and S. Jacquemoud, "Surface roughness retrieval by inversion of the Hapke model: A multiscale approach," *Icarus*, vol. 290, pp. 63–80, 2017.
[14] M. K. Shepard and P. Helfenstein, "A laboratory study of the bidirectional reflectance from particulate samples," *Icarus*, vol. 215, no. 2, pp. 526–533, 2011.
[15] M. K. Shepard and R. E. Arvidson, "The Opposition Surge and Photopolarimetry of Fresh and Coated Basalts," *Icarus*, vol. 141, no. 1, pp. 172–178, 1999. [Online]. Available: http://www.sciencedirect.com/science/article/pii/S001910359996150X
[16] J. D. Harms, C. M. Bachmann, B. Ambeau, J. W. Faulring, A. J. Ruiz Torres, G. Badura, and E. Myers, "Fully automated laboratory and field-portable goniometer used for performing accurate and precise multiangular reflectance measurements," *Journal of Applied Remote Sensing*, vol. 11, no. 4, pp. 046 014–15, 2017.
[17] S. R. Sandmeier, "Acquisition of bidirectional reflectance factor data with field goniometers," *Remote Sensing of Environment*, vol. 73, no. 3, pp. 257–269, 2000.
[18] B. Hapke, D. DiMucci, R. Nelson, and W. Smythe, "The cause of the hot spot in vegetation canopies and soils: Shadow-hiding versus coherent backscatter," *Remote Sensing of Environment*, vol. 58, no. 1, pp. 63–68, 1996.
[19] G. Schaepman-Strub, M. E. Schaepman, T. H. Painter, S. Dangel, and J. V. Martonchik, "Reflectance quantities in optical remote sensing-definitions and case studies," *Remote Sensing of Environment*, vol. 103, no. 1, pp. 27–42, 2006.
[20] M. J. Westoby, J. Brasington, N. F. Glasser, M. J. Hambrey, and J. M. Reynolds, "'Structure-from-Motion' photogrammetry: A low-cost, effective tool for geoscience applications," *Geomorphology*, vol. 179, pp. 300–314, 2012.
[21] C. Kazmierowski, J. Ceglarek, J. Cierniewski, and J. Jasiewicz, "Soil surface roughness quantification using DEM obtained from UAV photogrammetry," *Geomorphometry*, 2015. [Online]. Available: https://www.researchgate.net/publication/278848690
[22] C. Wu, S. Agarwal, B. Curless, and S. M. Seitz, "Multicore bundle adjustment," in *Proceedings of the IEEE Computer Society Conference on Computer Vision and Pattern Recognition*, 2011, pp. 3057–3064.
[23] C. Wu, "Towards linear-time incremental structure from motion," in *Proceedings - 2013 International Conference on 3D Vision, 3DV 2013*, 2013, pp. 127–134.
[24] Y. Furukawa, B. Curless, S. M. Seitz, and R. Szeliski, "Towards internet-scale multi-view stereo," in *Proceedings of the IEEE Computer Society Conference on Computer Vision and Pattern Recognition*, 2010, pp. 1434–1441.
[25] J. Cierniewski, C. Kaźmierowski, and S. Królewicz, "Evaluation of the Effects of Surface Roughness on the Relationship Between Soil BRF Data and Broadband Albedo," *IEEE Journal of Selected Topics in Applied Earth Observations and Remote Sensing*, 2015.
[26] C. Bachmann, R. Eon, B. Ambeau, J. Harms, G. Badura, and C. Griffo, "Modeling and intercomparison of field and laboratory hyperspectral goniometer measurements with G-LiHT imagery of the Algodones Dunes," *Journal of Applied Remote Sensing*, vol. 12, no. 1, 2017.
[27] D. C. F. Lo Presti, S. Pedroni, and V. Crippa, "Maximum dry density of cohesionless soils by pluviation and by ASTM D 4253-83. A comparative study," *Geotechnical Testing Journal*, vol. 15, no. 2, pp. 180–189, 1992.
[28] F. Mancini, M. Dubbini, M. Gattelli, F. Stecchi, S. Fabbri, and G. Gabbianelli, "Using unmanned aerial vehicles (UAV) for high-resolution reconstruction of topography: The structure from motion approach on coastal environments," *Remote Sensing*, vol. 5, no. 12, pp. 6880–6898, 2013.
[29] D. T. Lee and B. J. Schachter, "Two algorithms for constructing a Delaunay triangulation," *International Journal of Computer & Information Sciences*, vol. 9, no. 3, pp. 219–242, 1980.
[30] H. Kuipers, "A relief meter for soil cumulative studies," *Neth. J. Agric. Sci.*, vol. 5, no. 4, pp. 255–262, 1957.
[31] H. Croft, K. Anderson, and N. J. Kuhn, "Reflectance anisotropy for measuring soil surface roughness of multiple soil types," *Catena*, vol. 93, pp. 87–96, 2012.
[32] W. R. Clavano, "Reflectance change due to surface roughness–with applications to ocean optics," *Dissertation*, 2007.
[33] M. K. Shepard and B. A. Campbell, "Shadows on a Planetary Surface and Implications for Photometric Roughness," *Icarus*, vol. 134, pp. 279–291, 1998. [Online]. Available: http://linkinghub.elsevier.com/retrieve/pii/S0019103598959589

PLACE PHOTO HERE

Gregory Badura Gregory Badura is currently pursuing a PhD in Imaging Science at the Rochester Institute of Technology. His research interests include radiative transfer modeling of soils and vegetation, digital elevation model analysis, and hyperspectral image analysis.

PLACE PHOTO HERE

Charles M. Bachmann received the A.B. in physics from Princeton University (1984) and the Sc.M. (1986) and Ph.D. (1990) in physics from Brown University. He was a research physicist (1990−2013) at the Naval Research Laboratory, serving as Head of the Coastal Science and Interpretation Section in the Remote Sensing Division (2003 − 2013). From 2012−2013, through the US Navy Engineer and Scientist Exchange Program, he was at the Defence Science Technology Organisation (DSTO) Maritime Division, Sydney, Australia. In 2013, he joined the faculty of the Rochester Institute of Technology (RIT) Chester F. Carlson Center for Imaging Science (CIS) as the Frederick and Anna B. Wiedman Chair. Since 2016, he has also served as CIS Graduate Program Coordinator. His research focuses on hyperspectral remote sensing of coastal and desert environments, BRF and radiative transfer modeling for retrieval of geophysical and biophysical parameters, field calibration and validation, the development of advanced instrumentation (goniometers), as well as abstract models for interpreting hyperspectral and multi-sensor imagery based on manifold descriptions and graph theory. He holds two U.S. Patents for methods of analysis related to hyperspectral remote sensing imagery.